UC Irvine
UC Irvine Previously Published Works

Title

An observation-based, reduced-form model for oxidation in the remote marine troposphere.

Permalink

https://escholarship.org/uc/item/6x0852rh

Journal

Proceedings of the National Academy of Sciences, 120(34)

Authors

Baublitz, Colleen

Fiore, Arlene

Ludwig, Sarah

et al.

Publication Date

2023-08-22

DOI

10.1073/pnas.2209735120

Peer reviewed

An observation-based, reduced-form model for oxidation in the remote marine troposphere

Colleen B. Baublitz[a,b,1,2] (ID), Arlene M. Fiore[a,b,3] (ID), Sarah M. Ludwig[a,b] (ID), Julie M. Nicely[c,d] (ID), Glenn M. Wolfe[d] (ID), Lee T. Murray[e] (ID), Róisín Commane[a,b] (ID), Michael J. Prather[f] (ID), Daniel C. Anderson[d,g] (ID), Gustavo Correa[b] (ID), Bryan N. Duncan[d], Melanie Follette-Cook[d,h], Daniel M. Westervelt[b,i] (ID), Ilann Bourgeois[j,k,4,5] (ID), William H. Brune[l] (ID), T. Paul Bui[m], Joshua P. DiGangi[n] (ID), Glenn S. Diskin[n] (ID), Samuel R. Hall[o] (ID), Kathryn McKain[j,p] (ID), David O. Miller[l], Jeff Peischl[j,k] (ID), Alexander B. Thames[l,6], Chelsea R. Thompson[j,k], Kirk Ullmann[o] (ID), and Steven C. Wofsy[q]

The hydroxyl radical (OH) fuels atmospheric chemical cycling as the main sink for methane and a driver of the formation and loss of many air pollutants, but direct OH observations are sparse. We develop and evaluate an observation-based proxy for short-term, spatial variations in OH ($Proxy_{OH}$) in the remote marine troposphere using comprehensive measurements from the NASA Atmospheric Tomography (ATom) airborne campaign. $Proxy_{OH}$ is a reduced form of the OH steady-state equation representing the dominant OH production and loss pathways in the remote marine troposphere, according to box model simulations of OH constrained with ATom observations. $Proxy_{OH}$ comprises only eight variables that are generally observed by routine ground- or satellite-based instruments. $Proxy_{OH}$ scales linearly with in situ [OH] spatial variations along the ATom flight tracks (median r^2 = 0.90, interquartile range = 0.80 to 0.94 across 2-km altitude by 20° latitudinal regions). We deconstruct spatial variations in $Proxy_{OH}$ as a first-order approximation of the sensitivity of OH variations to individual terms. Two terms modulate within-region $Proxy_{OH}$ variations—water vapor (H_2O) and, to a lesser extent, nitric oxide (NO). This implies that a limited set of observations could offer an avenue for observation-based mapping of OH spatial variations over much of the remote marine troposphere. Both H_2O and NO are expected to change with climate, while NO also varies strongly with human activities. We also illustrate the utility of $Proxy_{OH}$ as a process-based approach for evaluating intermodel differences in remote marine tropospheric OH.

atmospheric oxidation | marine troposphere | tropospheric chemistry | hydroxyl radical

As the primary sink for methane, a strong greenhouse gas and air pollutant precursor, the hydroxyl radical (OH) is an influential yet poorly quantified lever on methane variations. Uncertainty in OH interannual variations is sufficiently high that it can hinder attribution of annual methane fluctuations. For example, inverse modeling analyses suggested several—sometimes conflicting—source sectors could explain the observed stabilization in methane levels from 2000 to 2005 (1–5), while uncertainty in the OH sink hinders effective trend attribution (6–8). Declining OH due to COVID-19 lockdowns has been invoked as a cause of the record-breaking increase in methane concentration observed since 2020 (9). The lack of constraints on OH also affects its representation in models that are applied to project future atmospheric composition and climate. Even when using the same emission inventories, chemistry-climate models simulate different methane lifetimes (10, 11), global mean OH (12, 13), and OH sensitivity to its drivers (13–15). Here, we develop and evaluate a proxy ($Proxy_{OH}$) built from OH steady-state chemistry over the remote marine troposphere. $Proxy_{OH}$ maps spatial variations in OH and can also be deconstructed to infer the processes contributing to OH fluctuations, information that extends beyond the capacity of existing proxies.

Sharp spatiotemporal variations in OH confound the development of a representative measurement network. Interannual variability in global (16–19) or hemispheric (20) mean OH is typically inferred using the loss rate of relatively long-lived, well-mixed chemicals that react principally with OH, such as methyl chloroform (21–23). Formaldehyde, an intermediate product of methane oxidation with a lifetime of several hours, shows promise for reflecting daily OH fluctuations at the relatively small scale of a tropospheric column (24, 25). Although they offer much-needed information on OH variability, none of the existing proxies provides insight into the individual photochemical processes controlling OH.

We use an unprecedented set of observations from the NASA Atmospheric Tomography (ATom) airborne campaign (26). This dataset, comprising 146,494 10-s average air parcels

Significance

The hydroxyl radical (OH) controls tropospheric methane loss rates. Global or hemispheric annual mean methane loss rates are currently inferred from observations of well-mixed gases, such as methyl chloroform. The short OH lifetime (1 to 2 s) and associated sharp spatiotemporal variations limit constraints on global models and understanding of "why" globally integrated OH fluctuates. From airborne measurements and steady-state chemistry, we develop a proxy to infer OH spatial variations and their sensitivity to individual photochemical drivers over 30 different regions in the remote marine troposphere. Two terms, water vapor and nitric oxide, contribute most of the within-region proxy variations, implying that a limited set of observations could serve as bellwethers of changing atmospheric oxidation patterns.

[1]To whom correspondence may be addressed. Email: cbb2158@columbia.edu.

[2]Present address: US Environmental Protection Agency, Research Triangle Park, NC 27709.

[3]Present address: Department of Earth and Planetary Sciences, Massachusetts Institute of Technology, Cambridge, MA 02139.

[4]Present address: Plant Ecology Research Laboratory, Ecole Polytechnique Fédérale de Lausanne, Lausanne CH-1015, Switzerland.

[5]Present address: Extreme Environments Research Laboratory, Ecole Polytechnique Fédérale de Lausanne Valais Wallis, Sion CH-1951, Switzerland.

[6]Present address: Department of Geosciences, Pennsylvania State University, University Park, PA 16802.

(27), offers the most spatially comprehensive set of in situ profile measurements of OH and its chemical and radiative drivers to date (28). In general, we subset the relatively unpolluted, remote marine tropospheric data into regional bins to account for large-scale vertical and latitudinal variations in OH. We first consider potential formulations of Proxy$_{OH}$ using a chemical box model (the Framework for 0-D Atmospheric Modeling, F0AM) constrained to the ATom observations (24, 29). Then we calculate Proxy$_{OH}$ directly from the observations and evaluate it against ATom [OH]. While there is a rich history of using box models constrained by airborne data to examine OH and its sensitivities to individual photochemical drivers (e.g., refs. 30–34), we instead calculate the proxy directly from observations and laboratory-measured kinetic rate coefficients (35) using only eight variables (Section 2.1.1). This differs from other analyses that, for example, calculate daily average methane loss rates in models constrained by ATom observations (36).

Proxy$_{OH}$ serves as a reduced-form model that offers a first-order estimate of the sensitivity of OH spatial variations to individual reaction rates or variables over the remote marine troposphere. We show below that Proxy$_{OH}$ suggests that two key drivers, water vapor (H_2O) and nitric oxide (NO), contribute most to regional variations in OH observed during the ATom campaign. We also apply Proxy$_{OH}$ to evaluate the simulated abundance and sensitivity of OH spatial variations in a global model used to project future composition and climate.

1. Results

1.1. Proxy Formulation over the Remote Marine Troposphere.
We define variations in OH as the spread in concentration at a specified spatiotemporal scale. Our goal is to distill the representation of OH to terms (e.g., photolysis rates or chemical species) that individually shape local OH distributions and, when combined, collectively capture measured OH variations. We use the F0AM photochemical box model constrained with ATom observations to test potential formulations of a proxy for OH spatial variations (Section 2.1.2).

Relatively few processes dominate OH variations over long timeframes or large spatial scales (37–39). Five years of OH measurements from a site in southern Germany suggest that insolation largely controls its temporal variations (40). Modeled global annual mean OH scales as a simple function of the ratio of reactive nitrogen and carbon emissions from preindustrial times to present-day (41). When combined with atmospheric humidity and overhead ozone columns, a proxy constructed from these four variables alone can capture global mean OH changes on glacial-interglacial (42) and decadal (13) timescales. Column-based satellite retrievals of species serving as OH sources and sinks reflect interannual modeled OH variations across U.S. cities from 2005 to 2014 (43) and to within 20 to 30% over the oceanic mid-troposphere from 2008 to 2017 (44). Here, we build on these previously identified sets of OH drivers to develop a proxy from observable quantities that reflect OH variations over smaller regional scales. We seek the simplest possible formulation that correlates strongly with ATom-measured [OH], so that Proxy$_{OH}$ may also serve as a reduced-form model. The advantage of a reduced-form model is that it can infer the relative importance of specific chemical species or reactions in contributing to variations in observed or simulated OH.

Locally, [OH] should be at steady state (OH production rate = OH loss rate) on timescales that exceed the OH lifetime of ~1 to 2 s (37). Over much of the troposphere, OH production is dominated by the reactions between singlet D atomic oxygen (produced from

ozone photolysis) and water vapor (O(^{1}D) + H_2O) and the hydroperoxyl radical with nitric oxide (HO$_2$ + NO), while losses are dominated by carbon monoxide (CO) and, secondarily, methane (38). We confirm that these two dominant production pathways capture spatial variations in OH production with the F0AM box model. In F0AM, the sum of the O(^{1}D) + H_2O and HO$_2$ + NO production rates strongly covary across the full ATom dataset with the total OH production rate ($\sum P_{OH}$; r^2 = 0.98) and account for 60% of $\sum P_{OH}$ (related to the slope of the regression between the proxy production rates and $\sum P_{OH}$ regression slope; m = 0.75). The tight fit between OH and the sum of the two largest production terms, even though these terms cumulatively comprise only 60% of $\sum P_{OH}$, implies that O(^{1}D) + H_2O and HO$_2$ + NO covary with other terms that contribute to $\sum P_{OH}$. We show example correlated reactions included in F0AM in *SI Appendix*, Table S1. The O(^{1}D) + H_2O and HO$_2$ + NO pathways, plus the HO$_2$ + O$_3$ reaction and the photolysis of hydrogen peroxide (H_2O_2) and methyl hydroperoxide (CH$_3$OOH) cumulatively represent 98% of $\sum P_{OH}$ (m increases to 0.98), with all other processes contributing <1% to $\sum P_{OH}$ individually. While including additional OH production processes beyond the two dominant pathways increases the slope to approach 1, it has little influence on the fit between the simplified representation of production and $\sum P_{OH}$ ($\Delta r^2 < 0.01$). This general pattern holds on smaller scales; the correlation coefficient between the sum of the O(^{1}D) + H_2O and HO$_2$ + NO with $\sum P_{OH}$ is r^2 = {0.97, 0.98} over the Pacific or Atlantic, respectively, and the median (r^2_{Mdn}) is 0.98 across smaller regional domains of 2 km by 20° latitudinal bins (Section 2.1.3). The composition of $\sum P_{OH}$ also generally holds over smaller scales (*SI Appendix*, Fig. S1). Thus, we adopt a simplified proxy representation of OH production that includes only the O(^{1}D) + H_2O and HO$_2$ + NO reactions (Eq. **1**). Note that this formulation does not rely on the relatively uncertain NO$_2$ measurement (36).

$$P_{OH} = \frac{2J_{O(^1D)}k_{O(^1D)+H_2O}[O_3][H_2O]}{k_{O(^1D)+M}[M] + k_{O(^1D)+H_2O}[H_2O]} \quad [\mathbf{1}]$$
$$+ k_{HO_2+NO}[HO_2][NO].$$

The OH sink terms also range in integration timescales. Within a parcel, OH loss to more reactive chemical species can fluctuate rapidly, on the order of minutes (e.g., OH + HO$_2$) to hours (e.g., OH + isoprene). CO or methane, the dominant OH sinks over the remote troposphere, may not vary within a parcel because their lifetimes range from months to years, though transport can produce sharp gradients across neighboring air parcels. The most appropriate terms to represent OH loss will thus vary with the local chemical regime and spatiotemporal scale under consideration.

To determine which loss pathways to include in the proxy, we consider the component of OH loss that is independent of its concentration, the "OH reactivity," denoted k'_{OH}. We focus on the 2-km altitude by 20° latitudinal regional bins before considering oceanic scales or all ATom observations together. Within the regional bins, F0AM indicates that CO is the largest contributor to the magnitude of $\sum k'_{OH}$ in each bin (22 to 53%), followed by CH$_4$ (9 to 22%). This holds everywhere except the southern tropical lower troposphere, where CH$_3$OOH reactivity is maximum at 20% (*SI Appendix*, Fig. S2). CO reactivity spatially covaries with $\sum k'_{OH}$ (r^2_{Mdn} = 0.45) within the 2-km altitude by 20° latitudinal bins more than does methane reactivity (r^2_{Mdn} = 0.22). The reactivities of HO$_2$, H_2O_2, and small, shorter-lived VOCs like formaldehyde (HCHO), CH$_3$OOH, or methanol (CH$_3$OH)

frequently correlate most strongly with $\sum k'_{OH}$ over this regional scale (*SI Appendix*, Fig. S3). However, they also moderately correlate with CO in any given regional bin (r^2 of approximately 0.3 to 0.5; *SI Appendix*, Fig. S4). Thus, the regional analysis suggests that, among all OH sink terms, CO contributes most to both the magnitude and spatial variations of $\sum k'_{OH}$ across the remote marine troposphere, as it often covaries with other OH sinks.

When considering all ATom observations together or when subsetting for the Pacific, methane reactivity emerges as a better predictor of $\sum k'_{OH}$ variations than other sinks, including CO (*SI Appendix*, Fig. S5). The methane and CO reactivities correlate across the full ATom dataset ($r^2 = 0.58$). Although using both CO and methane reactivity slightly improves the slope of the regression with $\sum k'_{OH}$ (with CO reactivity alone, m = 0.24; when summing CO and methane reactivities, m = 0.37), it does not substantially improve the correlation either over the full dataset or within a given oceanic basin ($\Delta r^2 \leq 0.05$). We therefore opt for simplicity and represent the OH sink term using only the CO reactivity, or equivalently, the lifetime of OH against its reaction with CO (denoted $\tau_{OH,CO}$, Eq. **2**).

$$\tau_{OH,CO} = \frac{[OH]}{k_{co+OH}[CO][OH]} = \left(k_{co+OH}[CO]\right)^{-1}. \quad [2]$$

As a simplified version of OH steady-state chemistry in the remote marine troposphere, Proxy$_{OH}$ is a reduced-form model for OH comprising the sum of the O(^{1}D) + H$_2$O and HO$_2$ + NO reactions scaled by $\tau_{OH,CO}$ (Eq. **3**).

$$\text{Proxy}_{OH} = P_{OH}\tau_{OH,CO}. \quad [3]$$

Combining the ATom observations directly with reaction rate coefficients (35), we demonstrate that alternative proxy formulations do not improve upon the Proxy$_{OH}$ fit with measured OH spatial variations (Section 1.2), though some formulations provide more comprehensive insight into the observed OH magnitude (Section 1.3). The remainder of this manuscript uses the ATom measurements directly (in other words, the F0AM box model is not used).

1.2. Proxy$_{OH}$ Captures Much of the ATom-Observed Variations in OH.

We assess the skill of Proxy$_{OH}$, calculated directly from the ATom observations, in predicting measured OH variations within each bin of our regional domain (Fig. 1 and Sections 2.1.1 and 2.1.3). We fit the Proxy$_{OH}$-[OH] regression slope and intercept within each bin using a Bayesian mixed-effects model implemented with Markov Chain Monte Carlo (MCMC) simulations (Section 2.2). The altitude and latitude are random effects in this mixed-effects model. The Bayesian approach offers an advantage over a frequentist method (e.g., ordinary least square regression, among other maximum likelihood approaches) because it evaluates distributions of Proxy$_{OH}$ and [OH] that account for the instruments' uncertainties. "True" values for OH and the proxy terms (i.e., $J_{O(^1D)}$ and the concentrations of H$_2$O, HO$_2$, NO, etc.) are drawn from normal distributions with mean and variance defined by the measured concentration and error, respectively. The posterior distributions, Proxy$_{OH,true}$ and [OH]$_{true}$), are used to assess the Proxy$_{OH}$ predictive skill quantified by the coefficient of determination and slope and intercept regression parameters. For comparison, *SI Appendix*, Fig. S6 shows these parameters when derived by an ordinary least squares regression, without accounting for measurement uncertainty, and the sample size and Proxy$_{OH}$ and [OH] value ranges within each spatial bin (the subplot axes in *SI Appendix*, Fig. S6 are the same as in Fig. 1). A comparison of the coefficient of determination (subplot background colors) *SI Appendix*, Fig. S6 demonstrates that the Bayesian mixed-effect approach (Fig. 1*A*) places less emphasis than ordinary least square regressions (*SI Appendix*, Fig. S6*A*) on few points distant from the data's primary mode of variation (for example, in subplots over the Pacific between −60° and −40°N and above 2 km).

The Proxy$_{OH}$-[OH] within-bin covariation is generally robust, with a median coefficient of determination (r^2_{Mdn}) across all spatial bins of 0.90 (IQR = 0.80 to 0.94). It is highest between 2- to 8-km altitude (r^2_{Mdn} = 0.93, IQR = 0.87 to 0.95) and over the Northern Hemisphere (r^2_{Mdn} = 0.93, IQR = 0.88 to 0.95). The proxy skill is expected to degrade where processes that are not included in its formulation affect OH variations. For example, convection may affect OH variations, potentially due to lofted peroxides (45), in
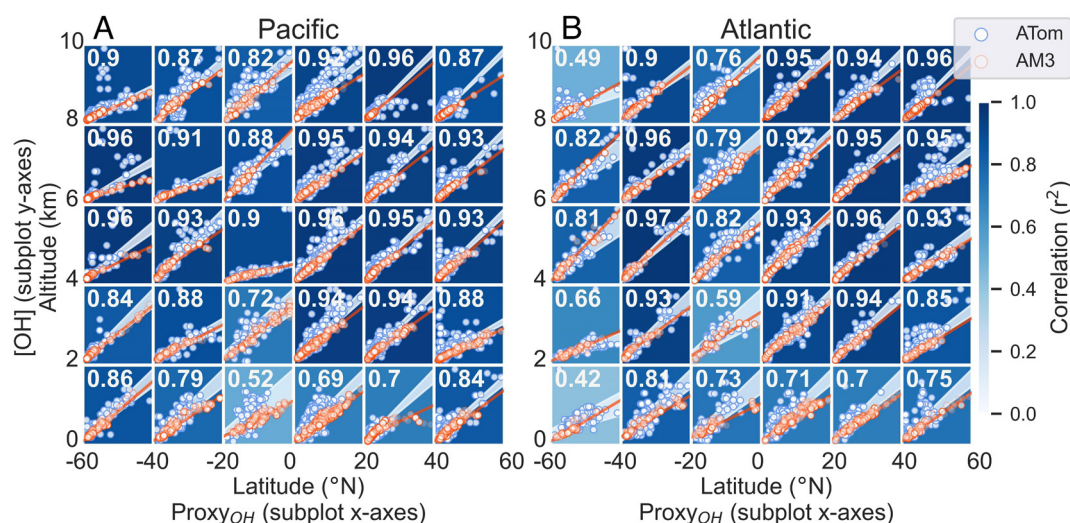
Fig. 1. The steady-state proxy for OH (Proxy$_{OH}$) captures much of the in situ measured and modeled [OH] variations along the ATom flight tracks. Shown is the spatial distribution over the (*A*) Pacific and (*B*) Atlantic oceans of the ATom-observed (blue dots) or AM3 modeled (orange dots) regression between Proxy$_{OH}$ and [OH] (both in ppt). The background color and number in the upper left corner of each subplot indicates the mean r-squared coefficient of determination (r^2) of the ATom Proxy$_{OH}$-[OH] posterior distributions, and the light blue shading illustrates the 95% Bayesian credible interval (Section 2.2). The model correlation is not shown but is slightly higher than observed (see text). The orange line is the AM3 Proxy$_{OH}$-[OH] ordinary least square regression. See *SI Appendix*, Fig. S6 for axes' descriptions.

some midlatitude plumes above 4 km (*SI Appendix,* Fig. S7). The comparably weaker fit in the lower troposphere may stem from marine-emitted halogens affecting the oxidation regime (46–48). However, the residuals of the Proxy$_{OH}$-[OH] regression do not show a systematic relationship (spatial median $r^2 \leq 0.03$) with other variables that affect oxidation (e.g., particle number concentration, halogens, convection; *SI Appendix,* Table S2). Overall, the aircraft observations suggest that Proxy$_{OH}$ reflects observed OH spatial variations on smaller scales than has previously been possible to discern using existing, globally well-mixed proxies.

In Section 1.1, the F0AM simulations indicated that alternate forms of a steady-state proxy over the 2-km altitude by 20° latitude bins could employ the OH lifetime against small oxidized carbon compounds (e.g., HCHO and CH$_3$OOH, which are included in the 10-s ATom observations; *SI Appendix,* Figs. S2 and S3) in place of, or in combination with, $\tau_{OH,CO}$. However, using the ATom observations directly to assess alternative proxy formulations that use these variables indicates that the simplest proxy formulation, using only CO as in Fig. 1, best reflects OH variations over the regional domain (*SI Appendix,* Table S3).

On larger scales, Proxy$_{OH}$ demonstrates similar predictive skill in reflecting OH variations when all observations in the domain are considered together (ordinary least squares $r^2 = 0.52$) as when subsetting for the Pacific or Atlantic ($r^2 = 0.49$ or 0.60, respectively). Replacing $\tau_{OH,CO}$ in Eq. 3 with the OH lifetime against methane $[= (k_{CH_4+OH} [CH_4])^{-1}]$ does not improve the correlation across all flight tracks ($r^2 = 0.44$), even when representing the OH sink in the proxy denominator as the sum of both rates ($r^2 = 0.51$). Despite the role of methane in modulating the global OH abundance, including it in Proxy$_{OH}$ does not improve the fit with observed OH because methane reactivity does not spatially covary with the total OH sink.

1.3. Inferring the ATom-Observed OH Abundance. While the coefficient of determination describes the extent to which the proxy fits the observed *variations* in ATom [OH], the intercept and slope infer the *magnitude* of the proxy in comparison with [OH]. When considering all data together, the Proxy$_{OH}$-[OH]

intercept overlaps zero, averaging 0.05 ± 0.05 ppt ($\mu \pm 95\%$ CI), though the intercept is generally positive within a given bin (Fig. 2 *A* and *B*). A positive intercept indicates a small missing background source or underestimated sink, though the within-bin MCMC mean intercept does not correlate with the mean of the processes considered for the residual analysis (across bins, $r^2 \leq 0.14$; *SI Appendix,* Table S2). The strongest residual relationship is shown with CH$_3$OOH, the probability of convective influence, and solar zenith angle. This suggests that Proxy$_{OH}$ could potentially be refined to reduce the regression intercept by accounting for the lofting and photolysis of CH$_3$OOH.

The Proxy$_{OH}$-[OH] slope overall averages to 0.39 ± 0.25. It generally maximizes below 4 km and at higher latitudes, particularly in the northern hemisphere, and minimizes in the upper troposphere (Fig. 2 *C* and *D* and *SI Appendix,* Fig. S9). The slope reflects the relative contribution of Proxy$_{OH}$ terms to total OH production and loss (*SI Appendix,* Fig. S8). For example, a larger slope could indicate that the Proxy$_{OH}$ production terms encompass more of the total OH production; alternatively, but not exclusively, it could suggest that the Proxy$_{OH}$ loss terms encompass less of the total OH loss (refer to Section 1.1 and *SI Appendix,* Figs. S1 and S2). While the Proxy$_{OH}$ representation of the magnitude of both OH production and loss influence the regression slope, the slope is more tightly coupled with the contribution of CO to the total OH loss (compare *SI Appendix,* Fig. S8 *B* and *C*), stemming from a larger underestimate in the OH sink than in its source as part of the Proxy$_{OH}$ formulation (compare F0AM-simulated percent contributions in *SI Appendix,* Fig. S1 with *SI Appendix,* Fig. S2).

Including additional sink terms in the proxy formulation increases the slope (*SI Appendix,* Table S3 and Fig. S9), but as described in Section 1.2, it does not improve the [OH] fit (little change in r^2). Proxy$_{OH}$ only uses the OH lifetime against CO. Expanding to include the OH lifetime against HCHO ($k_{HCHO+OH}$[HCHO]) and/or CH$_3$OOH ($k_{CH3OOH+OH}$[CH$_3$OOH]) in the proxy sink term reduces the spatial gradients in the MCMC-simulated slopes (compare stars and squares to circles in *SI Appendix,* Fig. S9). The slope spatial gradients are smallest when
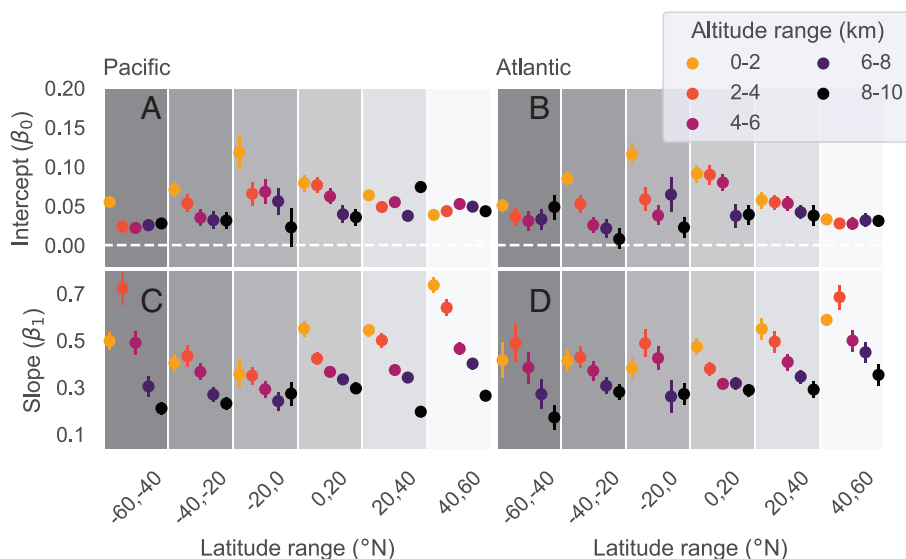
Fig. 2. The Proxy$_{OH}$-[OH] regression slope and intercept reflect the relationship between OH sources and sinks. The distinct spatial patterns in the regression parameters indicate that using the Proxy$_{OH}$ to infer the local OH concentration requires accounting for vertical and latitudinal distributions. Spatial distribution of the intercept (*Top*; *A* and *B*) and slope (*Bottom*; *C* and *D*) posteriors from the Bayesian linear regression between Proxy$_{OH}$ and observed [OH] are shown. Boxes span six 20° latitudinal bins (*x* axis and gradient in gray background color) and five 2-km altitude bins (color), separated by ocean basin (*Left* or *A* and *C*: Pacific; *Right* or *B* and *D*: Atlantic). For a given bin, the posterior is drawn as the final 1,000 iterations across three chains from Markov Chain Monte Carlo simulations used to implement the Bayesian fit (Section 2.2). Vertical colored lines indicate the 95% credible interval of the intercept and slope for that spatial bin.

including the OH lifetime against CH_3OOH (squares in *SI Appendix*, Fig. S9), although the spread (vertical bars) increases due to larger CH_3OOH measurement uncertainty. For all proxy formulations, the slope is generally smallest between 8- and 10-km altitude. In this vertical layer, *SI Appendix*, Fig. S1 indicates that H_2O_2 photolysis and the reaction of $HO_2 + O_3$ are often larger contributors to P_{OH} than $O(^1D) + H_2O$. Overall, this analysis suggests that changes in the composition of k'_{OH} generally drive the spatial variations in the slope, while missing sources may contribute most in the upper troposphere.

The $Proxy_{OH}$ underestimate of the total magnitude of the OH source and sink terms stems from its intended simplicity, such that one limitation of $Proxy_{OH}$ is that it does not represent the exact ratio of OH production to loss. However, the tight fit of the regression between $Proxy_{OH}$ and measured [OH] implies that the spatial distribution of slopes and intercepts derived here can be used to infer the total magnitude of [OH] over the remote marine troposphere (further discussion of the spatial variations in regression parameters is available in *SI Appendix*, Text S1).

1.4. Decomposing the Observation-Based Proxy to Evaluate the Sensitivity of OH Variations. We decompose $Proxy_{OH}$ across all ATom observations, by oceanic basin and within each altitude–latitude bin as a first-order estimate of the chemical sensitivity of OH variations to individual species and chemical production or loss pathways. This decomposition is a major advantage relative to existing OH proxies because it enables inference of the relative importance of different processes in contributing to spatial OH variations. Specifically, we construct sensitivity versions of the proxy in which we hold a single reaction rate (e.g., $O(^1D) + H_2O$) or term (e.g., NO or temperature, T) constant at its mean value per 2 km by 20° zonal bin, and then calculate the coefficient of determination (r^2) between $Proxy_{OH}$ and each sensitivity version to assess the change in fit ($1 - r^2$). This simple approach assumes a linear relationship between each term or rate and $Proxy_{OH}$. Because it neglects higher order chemical processes that may lead to nonlinear responses, the contributions summed across variables may not add to 100%. In addition, some of the drivers (*e.g.*, NO and ozone) may be correlated. Below we display the influence of rates or terms as their contribution to the total proxy fit ($1 - r^2$),

such that $1 - r^2$ approaching 1 indicates a rate or term with a strong influence on [OH] variations.

We first evaluate the role of individual terms composing $Proxy_{OH}$ in each of the 2-km altitude by 20° latitude subsets of the ATom observations. We find that H_2O dominates most of the ATom-observed $Proxy_{OH}$ variations (Fig. 3A), especially in the midtroposphere. This result is also robust when considering all ATom observations together or when subsetting by oceanic basin (*SI Appendix*, Table S4). Controls on proxy variations over either oceanic basin are shown in *SI Appendix*, Fig. S10. Our observation-based analysis affirms that, consistent with previous model-based analyses of the remote troposphere (37, 38), $O(^1D) + H_2O$ is most influential throughout much of the free troposphere, while $HO_2 + NO$ dominates in the upper troposphere and sometimes in the more polluted lower troposphere. In addition, our results are consistent with earlier work showing that several models constrained with ATom chemical observations attribute much of the difference in intermodel OH distributions to H_2O discrepancies (27). Further, climate model intercomparisons demonstrate biases in H_2O of ± 10% in the lower troposphere that increase to as much as ± 100% in the upper troposphere (49, 50). Convection and cloud microphysics have long challenged accurate simulations of water vapor vertical profiles (e.g., refs. 51–55). Our results reinforce that variations in OH are heavily tied to water vapor. Improving the accuracy of atmospheric hydrologic processes in chemistry-climate models should thus improve OH trend simulations, as well as those for methane, CO, and other trace gases whose primary sink is reaction with OH.

The water vapor feedback due to anthropogenic climate change could increase methane destruction by accelerating its loss through reaction with tropospheric OH (39). Global average OH has historically been well buffered (18) because its variability was dominated by anthropogenic combustion (41), which affects both its production (via NO and O_3) and loss (via CO and other forms of reactive carbon). However, rising atmospheric [H_2O] only directly affects OH production, in the absence of a compensating increase in the OH sink. A coupled chemical model would be necessary to account for the full effect of climate change on atmospheric oxidation, for example, due to offsetting feedbacks, like an increase in H_2O_2 production followed by deposition or weather-sensitive emissions such as
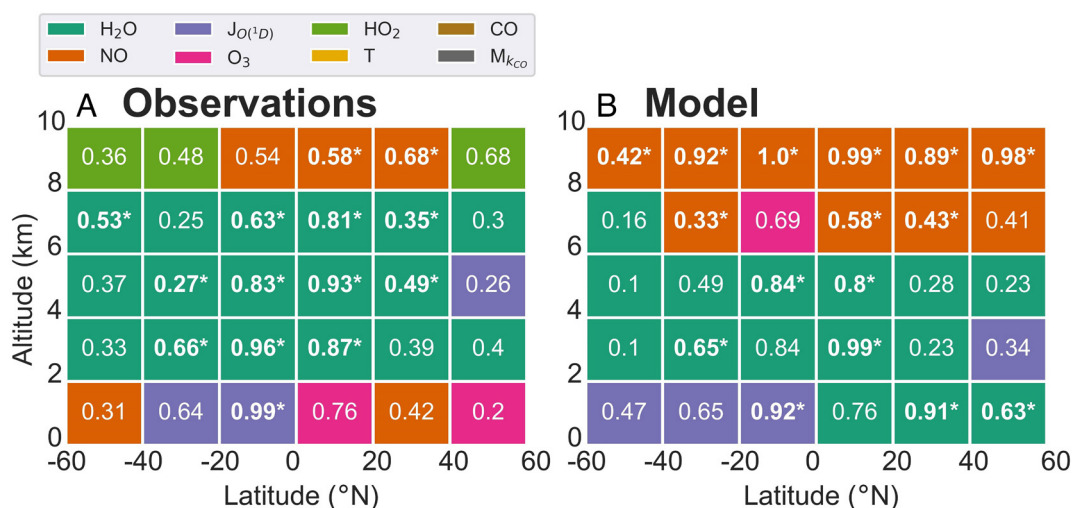
Fig. 3. Few terms—water vapor (H_2O), nitric oxide (NO), the hydroperoxy radical (HO_2), ozone (O_3) and the rate of O_3 photolysis to $O(^1D)$ ($J_{O(^1D)}$)—dominate the sensitivity of $Proxy_{OH}$ variations over the remote troposphere. Spatial distribution of the difference in the $Proxy_{OH}$-[OH] fit ($1 - r^2$) attributed to each of the physical or chemical terms that comprise $Proxy_{OH}$ H_2O, NO, HO_2, $J_{O(^1D)}$, O_3, temperature (T), CO or the pressure dependence of the CO reaction rate ($M_{k_{CO}}$) are individually held constant, for (*A*) ATom observations and (*B*) AM3 fields sampled along the ATom flight tracks. The colors indicate which of the terms is the largest contributor to proxy variance in that cell, with bold text and an asterisk indicating that the colored term contributes 0.20 more (r^2 units) than the next-most influential term.

methane from wetlands. Proxy$_{OH}$ instead offers a simple, first-order projection of how OH might respond to the expected rise in atmospheric water vapor abundances with future climate change. Applying the mean increase in water vapor between 2,010 and 2,100 from RCP 8.5 (56), used by Holmes et al. (39), we infer from Proxy$_{OH}$ that the projected magnitude of change in [H$_2$O] (42.3%) along the ATom flight tracks where H$_2$O dominates the OH sensitivity (between 2- and 8-km altitude) could increase regional average [OH] by 19%. This estimate indicates the potential for a large, negative feedback to climate change by increasing the methane sink. However, this sensitivity was derived from short-term, regional observations, and needs further study into the connection to long-term global trends. This approach also neglects nonlinear chemical feedbacks and potential simultaneous offsetting processes (e.g., an increase in methane). While additional work employing a more complex model is needed, this first-order estimate suggests that higher water vapor associated with anthropogenic climate change could cause a departure from the recent era, in which OH derived from globally well-mixed proxies has not shown a substantial trend since the start of the methyl chloroform record (18, 19, 57).

NO is the second-largest driver of within-bin Proxy$_{OH}$ spatial variations based on our analysis of the ATom observations over the remote marine troposphere (Fig. 3A and *SI Appendix*, Fig. S10). $J_{O(^1D)}$ sometimes dominates over midlatitude, lower tropospheric regions in the Southern Hemisphere. HO$_2$ emerges as influential in some regions, in particular when separating the data by oceanic basin (*SI Appendix*, Fig. S10 *A and C*). Ozone also affects the Proxy$_{OH}$ spatial variations in several bins, though not substantially more ($\Delta r^2 < 0.2$) than the next-most influential term (Fig. 3A). On larger scales, ozone is generally a stronger driver of Proxy$_{OH}$ spatial variations than NO, $J_{O(^1D)}$ or HO$_2$, while H$_2$O still dominates (*SI Appendix*, Table S4). The OH lifetime against CO does not dominate in any of the 2 km by 20° latitudinal bins or over larger spatial scales (*SI Appendix*, Table S4) likely due to the relatively long lifetime of CO. However, trends in CO sources may affect the OH sensitivity over longer timescales, for example, due to climate-driven changes in biomass burning emissions (58).

We compare a parallel decomposition of a more comprehensive proxy version with the terms that covary most strongly with Proxy$_{OH}$ (compare Fig. 3 and *SI Appendix*, Fig. S11). The expanded proxy includes additional terms affecting [OH] that were identified in previous sections as important for reconstructing the total OH abundance based on their contribution to the total OH source or sink (*SI Appendix*, Figs. S1 and S2 and Table S1) or an increased slope of the proxy-[OH] fit (*SI Appendix*, Fig. S9 and Table S3). Additional OH production terms are H$_2$O$_2$ photolysis and the reaction of HO$_2$ with O$_3$; OH sink terms are its reaction with methane, formaldehyde, and methyl hydroperoxide. Conducting the same sensitivity analysis, as in Fig. 3A, the same terms dominate the base and expanded proxy sensitivity analysis (*SI Appendix*, Fig. S11). We conclude that the base Proxy$_{OH}$ captures key terms for inferring within-bin OH spatial variations (compare bins with asterisks in Fig. 3 and *SI Appendix*, Fig. S11). This sensitivity analysis indicates that, even though some of the expanded proxy terms affect the magnitude of OH (e.g., CH$_3$OOH; see *SI Appendix*, Fig. S9), they are not as influential over OH spatial variations on these scales.

1.5. Evaluating a Chemistry-Climate Model Using Proxy$_{OH}$. We illustrate how Proxy$_{OH}$ can be used to evaluate the processes that control spatial OH variations in a chemistry-climate model. Paralleling our observation-based analysis, we construct Proxy$_{OH}$ from hourly fields archived from the GFDL AM3 chemistry-climate model for comparison with AM3-simulated OH

(Section 2.1.4). Proxy$_{OH}$-[OH] correlations in the global AM3 model sampled along the ATom flight tracks (orange points and line in Fig. 1) have a spatial median $r^2_{Mdn} = 0.95$, just above the interquartile range of the observationally derived r^2_{Mdn} (0.90, IQR = 0.80 to 0.94). The slightly tighter modeled relationship may reflect the different spatiotemporal coverage of the two datasets, or it could indicate a model underestimate in OH sink variations (59, 60). On larger spatial scales (here, considering the full ATom dataset), AM3 indicates the strength of relationship would be similar if the OH sink were represented through methane ($r^2 = 0.67$ for all ATom; $r^2 = 0.63$ or 0.71 over the Pacific or Atlantic, respectively) instead of CO ($r^2 = 0.65$, 63, or 0.75, respectively). Overall, we conclude that the link between OH production and [OH] is tighter in AM3, and in F0AM (refer to *SI Appendix*, Fig. S5), than in the observations due to an underestimate in the variability of OH reactivity, potentially due to missing OH loss processes (*SI Appendix*, Fig. S12).

Decomposing the modeled Proxy$_{OH}$ variations by individual terms, we find similar spatial patterns for within-bin relationships as in the observations, with some exceptions (Fig. 3B versus Fig. 3A). In both analyses, H$_2$O emerges as the most influential term in most of the 2 km by 20° latitude bins, especially in the mid-troposphere. NO dominates the within-bin Proxy$_{OH}$ variations in the upper troposphere, though the model simulates NO influence on Proxy$_{OH}$ variations over a larger swath of the upper troposphere (>6 km) than indicated by the measurements (>8 km). This overestimate is generally associated with a high normalized mean bias in NO (in other words, modeled NO is higher than observed; Section 2.1.4 and *SI Appendix*, Fig. S13), possibly indicating an error in low-temperature kinetic data for NO$_x$-O$_3$ photochemical cycling (61). Conversely, AM3 underestimates the extent of HO$_2$ influence over Proxy$_{OH}$ spatial variations in the upper troposphere, colocated with a low normalized mean bias in modeled HO$_2$ (*SI Appendix*, Fig. S14). AM3 also has a low bias in H$_2$O in this region (*SI Appendix*, Fig. S15).

The model also fails to capture the observed variability in the drivers of Proxy$_{OH}$ spatial variations in the lower troposphere. AM3 suggests that only $J_{O(^1D)}$ is influential across the Southern Hemisphere, while H$_2$O modulates modeled Proxy$_{OH}$ spatial variations throughout the Northern Hemisphere in this vertical layer. The observations, in contrast, limit the $J_{O(^1D)}$ influence to a smaller horizontal extent, and indicate that H$_2$O does not dominate spatial variations in any lower tropospheric region (Fig. 3A). When considering individual oceanic basins, H$_2$O emerges as a primary driver of Proxy$_{OH}$ variations over two lower tropospheric bins in the Atlantic (*SI Appendix*, Fig. S10). The model underestimates the sensitivity of Proxy$_{OH}$ spatial variations to NO in the lower troposphere, but the model NO bias differs in sign by hemisphere. We infer that, in the lower troposphere, modeled NO may be too low to drive Proxy$_{OH}$ variations in the Southern Hemisphere but is excessively high in the Northern Hemisphere, where Proxy$_{OH}$ variations may no longer be sensitive to NO.

The analysis above illustrates how Proxy$_{OH}$ can be used as a tool for rapid assessment of the relative importance of chemical processes that control tropospheric oxidation variations. This information can be applied to model evaluation, or to inform areas for exploration using more comprehensive, but more expensive, global chemistry-climate models. Overall, the modeled sensitivity of Proxy$_{OH}$ variations is consistent with the observations in demonstrating that few terms, mainly H$_2$O and NO, dominate the sensitivity of regional oxidation variations over the remote marine troposphere.

1.6. Discussion: Advancing Understanding of the Methane Lifetime Using Proxy$_{OH}$. Improved confidence in methane trend attribution relies on a better understanding of OH variations (62), but OH variations have been difficult to constrain, in part, because of nonlinear relationships between OH and its numerous underlying drivers. We develop and evaluate an observation-based proxy for subhemispheric spatial variations in OH (Proxy$_{OH}$) over the remote marine troposphere. Proxy$_{OH}$ is based on a simplified version of steady-state OH chemistry (two production and one loss pathway) that accounts for the contribution from key drivers to regional spatial variations in OH. By enabling a first-order approximation of the influence of individual variables on OH spatial variations, Proxy$_{OH}$ serves as a reduced-form model that can provide process-based insight into OH fluctuations.

Decomposing the ATom-observed Proxy$_{OH}$, calculated directly from the aircraft observations, suggests that few terms—H$_2$O and, to a lesser extent, NO—modulate almost all of the inferred OH variations over the remote marine troposphere on regional scales (i.e., 2-km altitude by 20° latitude bins). Thus production processes control the sensitivity of OH variations within a regional bin. On larger scales (i.e., across bins), the composition of OH reactivity modulates the regression slope, relevant for inferring the OH magnitude.

ATom, by design, flew over atmospheric swaths where chemistry is relatively pristine and homogeneous. Additional development of Proxy$_{OH}$ is needed over more polluted terrestrial regions, where higher NO$_x$ levels and more complex reactive carbon compounds should likely be included among the processes comprising Proxy$_{OH}$ (e.g., HONO as a source or OH + NO$_2$ as a sink). Retrieving key Proxy$_{OH}$ variables from satellites should also advance understanding of OH, at least on a column basis. For example, H$_2$O is currently measured directly (63) while NO or $J_{O(^1D)}$ may be inferred (64–67) using space-based instrumentation. In a similar vein, machine learning (ML) has already been applied to approximate long-term trends in OH using chemical transport model simulations and satellite retrievals in urban environments over North America (43). This analysis found that a similar set of variables to those included in Proxy$_{OH}$ contribute most of the variation in temporal trends in model OH over several North American cities (noting that HCHO was more influential than the CO included in Proxy$_{OH}$ in these relatively polluted terrestrial environments). While this ML approximation is yet to be evaluated against OH observations, these results indicate promise for the rapid development of alternative possible formulations for Proxy$_{OH}$ over a range of conditions. At the same time, our method could be applied to evaluate ML approximations, potentially by mining previous airborne observations of OH for in situ constraints on environment-specific formulations of Proxy$_{OH}$ (a comprehensive compilation of ATHOS OH measurements is available in ref. 34).

Our analysis using in situ observations suggests that future column-based applications of Proxy$_{OH}$ should account for the vertical and latitudinal distribution of the relationship between this proxy and OH, for which we estimated initial slope and intercept values over the remote marine troposphere. A column-based proxy should also consider the distribution of temperature and pressure in the representation of reaction rate constants. A satellite-observed form of Proxy$_{OH}$, especially in combination with HCHO retrievals that map column OH variations (24, 25), could offer a spatially expansive dataset for inference of not only the OH abundance but also its sensitivity to key drivers of atmospheric oxidation. By placing much-needed constraints on the methane sink via reaction with tropospheric OH, this knowledge will improve confidence in the interpretation of observed methane trends as well as future projections under global change.

By offering insight into the sensitivity of OH spatial variations to individual OH source and sink terms, Proxy$_{OH}$ serves as a process-based, simple model that bridges point measurements and global atmospheric chemistry model simulations. Across global models, the decadal mean OH concentration shows a linear relationship with a combination of $J_{O(^1D)}$, specific humidity and the source of nitrogen and carbon (13). Here, we demonstrate that an observation-based version of this combination of variables, Proxy$_{OH}$, maintains a linear relationship with measured OH concentrations over regional scales in the remote marine troposphere. Our observation-based results suggest that future evaluation of modeled tropospheric oxidation over global background regions, in particular over timescales shorter than the methane lifetime (12, 68), should target an accurate model representation of variations in H$_2$O and NO and their relationships with OH. As a test case of the steady-state proxy's potential to evaluate and interpret global models, we evaluate GFDL AM3 chemistry-climate model simulations sampled along the ATom flight tracks. The proxy decomposition identified a model mismatch in processes modulating OH in the upper-troposphere to midtroposphere and points to an underestimate in H$_2$O. Provided that diagnostics on the same spatiotemporal scales are available, our AM3 evaluation could be extended to additional models, so that Proxy$_{OH}$ may be applied to evaluate the representation of remote marine tropospheric OH and the species controlling its production and loss. A separate model analysis using the ATom data also concluded that intermodel differences in H$_2$O distributions lead to large differences in simulated methane loss rates along the ATom flight tracks (27). This shortcoming could undermine simulated relationships, for example between lightning and the NO$_x$ lifetime, which is a crucial component of accurate process-based representations of OH (13, 69–71). Probing Proxy$_{OH}$ thus provides insight into the sensitivity of OH variations to H$_2$O and NO, which would not have been apparent from conventional comparisons of measured and modeled H$_2$O or NO distributions.

We identify both H$_2$O and NO as key drivers of [OH] variations in the remote troposphere. Nevertheless, these two parameters do not fully explain the OH variability, and further investigation is recommended over a range of pollution regimes and environmental conditions. Both H$_2$O and NO are expected to respond to climate change and variability, while human activities like fossil fuel combustion also affect NO distributions. Climate studies have emphasized the need for additional constraints on H$_2$O vertical profiles because it is a critical feedback on the global energy budget in response to anthropogenic climate change (52–55). Here, we identify another rationale relevant for both climate and air quality: improved representation of the H$_2$O spatial distribution would facilitate a better understanding of the OH influence on the methane lifetime. Therefore, accurate characterization of regional H$_2$O and NO spatiotemporal distributions could advance our understanding of the effect of global change on atmospheric oxidation.

2. Materials and Methods

2.1. Observations and Model Simulations.

2.1.1. Aircraft Measurements. ATom deployed the NASA DC-8 aircraft to measure OH concentrations as well as several key drivers of OH production and loss rates: water vapor, actinic fluxes, and reactive carbon and nitrogen. ATom flew south along the center of the Pacific basin, following 180°W within ~15° longitude, and north along the center of the Atlantic basin, generally between 15° and 30°W (*SI Appendix*, Fig. S16). *SI Appendix*, Table S5 describes the measurements used in our analysis (72–88), which spans ATom-1, 2, 3, and 4, corresponding to Northern Hemisphere summer (28 July to 22 August, 2016), winter (26 January

to 22 February, 2017), fall (28 September to 26 October, 2017), and spring (24 April to 21 May, 2018).

2.1.2. Box Model Simulations. To provide further support for our observation-based proxy, we draw on 60-s average OH simulations along the ATom flight tracks from the Framework for 0-D Atmospheric Modeling (F0AM v.4, available at https://github.com/AirChem/F0AM/; ref. 29 with the Master Chemical Mechanism (MCM) version 3.3.1; ref. 89). A subset of MCM v3.3.1 is implemented within F0AM. The box model is constrained with the ATom data, including meteorological, radiative, and chemical variables following (30). Box model simulations of HO$_x$ (OH plus hydroperoxyl, HO$_2$) forced by measurements (excluding HO$_x$) along the ATom-1 and 2 flight tracks show consistency with ATom-1 and 2 observed HO$_x$ (24).

Data at 1 Hz time resolution are averaged to 1-min frequency and gap-filled via linear interpolation for gaps less than 5 min by correlating with CO for species with a correlation coefficient ($r \geq 0.7$) for all data within 500 m of aircraft altitude, and substituting data below an instrument's limit of detection (LOD) with 20% of the LOD concentration, as in previous box model applications (90). The following reactions are added to the F0AM chemical mechanism (MCM v3.3.1): CH$_4$+O(^{1}D), photolysis of HO$_2$NO$_2$, and CH$_3$O$_2$+OH (91). Box model simulations are performed for all data points where the CO and O$_3$ values are valid (following gap-filling) and where either or both NO and NO$_2$ are greater than zero. All flights from all four ATom deployments are simulated with the following exceptions: ATom-3 flight 20170928 (for which NO$_2$ measurements are missing), ATom-3 flights 20171014, 20171025, and 20171027 (for which photolysis measurements are missing), and ATom-4 flight 20180518 (a transit flight during which VOC measurements were not made).

The F0AM simulations are integrated with a 10-min time step to diurnal steady state, which occurs when the fractional change in short-lived species through a simulated solar cycle falls below 0.1%. Photolysis frequencies vary diurnally and are scaled to match the measured J-values at the local time of observation. All other constraints are held fixed throughout the simulation. A family constraint is imposed for NO$_x$, such that NO and NO$_2$ concentrations are allowed to fluctuate diurnally, while their sum remains fixed to that measured. A second simulation then adjusts the total NO$_x$ abundance, such that the resulting simulated NO concentration matches the observed NO, which is less susceptible to measurement artifacts than NO$_2$. This approach thus imposes an NO constraint while allowing NO and NO$_2$ to undergo diurnal variation during the simulation in a realistic manner.

2.1.3. Data Preparation. For much of our analysis, we spatially subset the ATom data, F0AM (Section 2.1.2) and AM3 simulations (Section 2.1.4) into a 2-km altitude by 20° latitudinal (~2,000 km) grid that spans 0 to 10 km and −60° to 60°N, including both ocean basins. We refer to the 0 to 2, 2 to 8, or 8 to 10-km altitude ranges as the lower, mid-, or upper troposphere and to the 0° to 20°, 20° to 40°, or 40° to 60° zonal ranges in either hemisphere as tropical, extratropical, or midlatitude, respectively. Referencing the previously calculated 0.25-km vertical by 6-km horizontal coverage per 30 s of ATom sampling (36), our spatial bins integrate approximately 4 min of vertical and 2 h of horizontal measurement, in comparison with the hourly timestep of our global model. For consistency, we use ATom data between 60°S and 60°N and below 10 km when considering larger spatial scales.

Within our domain, we filter the ATom data to exclude air masses with strong influence from biomass burning (CO concentration over 150 ppb, 2.2% of valid observed points), the stratosphere [water vapor (H$_2$O) mixing ratio below 10 ppm, 0.7% of valid data], low incident sun (solar zenith angle >80°, 7.0% of valid data) or anthropogenic pollution (high concentration outliers in NO, defined as above the 75th percentile plus three times the interquartile range in the log-transformed distribution for the spatial domain under consideration; 1.2% of valid observations together or 0 to 10% of each 2 km by 20° latitude bins). We also filter the F0AM and AM3 simulations using the same screening criteria applied to their respective model diagnostics. Because we are interested in the OH drivers and variations, we remove observations with a low signal-to-noise ratio, specifically with [OH] below the ATHOS limit-of-detection of 0.018 ppt (9.2% of observed or 9.0% of modeled points) and in which [NO] is less than its corresponding 2-sigma uncertainty (14% of observed points). To avoid interpreting noise as part of the observed Proxy$_{OH}$-[OH] relationship, we do not draw conclusions in air masses with very low [OH] or [NO]. Overall, we retain 74.7 to 74.9% of valid observations within our domain, depending on the spatial scale considered.

2.1.4. GFDL AM3 global chemistry-climate model simulations. We evaluate hourly fields for the variables that comprise Proxy$_{OH}$ (H$_2$O, NO, HO$_2$, etc.) from the National Oceanic and Atmospheric Administration (NOAA) Geophysical Fluid Dynamics Laboratory AM3 chemistry-climate model (14, 92, 93). AM3 has 48 vertical levels on a cubed sphere grid with approximately 2° by 2° horizontal resolution (14). Our base configuration, described previously (94–96), nudges the horizontal wind fields to the National Centers for Environmental Prediction Global Forecast System with a nudging strength that falls off with pressure (97). Global NO emissions total 44.7, 44.9 and 45.2 Tg N yr^{-1}, and CO emissions total 1221, 1223 and 1226 Tg yr^{-1} for the ATom years 2016, 2017, and 2018, respectively. MEGAN-simulated isoprene emissions are included in AM3, totaling 418, 395 and 394 (98, 99) Tg C yr^{-1} globally for 2016, 2017, and 2018, respectively. The anthropogenic and biomass burning emissions are drawn from the Representative Concentration Pathway 8.5 scenario (RCP 8.5; ref. 56) for the years spanning the ATom campaign (2016 to 2018) by interpolating between 2010 and 2020 values following (14). The global biomass burning emissions total 5.2 to 5.3 Tg N yr^{-1} for NO and 437 to 438 Tg CO yr^{-1} for each year overlapping with ATom.

We compare the model with ATom by sampling the grid cells containing the corresponding observed latitude, longitude, altitude, and time for each observed data point and evaluate AM3 using the normalized mean bias (Eq. **4**), in which i,obs and i,mod represent a 10-s average observation from ATom and the colocated hourly average model diagnostic from AM3, respectively. The AM3 $J_{O(^1D)}$ photolysis rates were previously shown to be consistent with CAFS observations over the tropical and northern Pacific ATom-1 flight tracks (100).

$$\text{Normalized mean bias}\,(\%) = \frac{\sum \left(x_{i,mod} - x_{i,obs} \right)}{\sum \left(x_{i,obs} \right)}. \qquad [\mathbf{4}]$$

2.2. Bayesian Mixed-Effects Model. Mixed-effects models are an extension of linear regression. For predictor variables, they combine a fixed effect (i.e., Proxy$_{OH}$) and random effect (a grouping variable or source of nonindependence; here, the arbitrary spatial bin selection). Previous atmospheric chemistry research has applied some form of mixed-effect model for applications such as mapping high-resolution urban pollution (101) or for cluster analysis of surface ozone episodes (102). For our project, it would be challenging to incorporate observational uncertainty using a frequentist (e.g., maximum likelihood) approach. Instead, we fit the mixed-effects model using a Bayesian regression, which incorporates measurement uncertainty while assessing the predictive strength and significance of fit. The model fits distributions of Proxy$_{OH}$ and [OH] that are sampled from the ATom observations combined with information regarding the instruments' uncertainty distributions. The true gas concentrations, and the Proxy$_{OH}$ derived from them, are considered to be unobserved but implicit ("latent") variables and are designated using the subscript true. Each true concentration is drawn from a normal distribution with mean and SD corresponding to the measured concentration and uncertainty (i.e., $P([X]_{true}|[X]_{Obs}, \sigma_x)$; uncertainties listed in *SI Appendix*, Table S6). *SI Appendix*, Fig. S17 illustrates the parameter relationships for the Bayesian mixed-effects model through a directed acyclic graph.

This approach was implemented in R using MCMC with the Just Another Gibbs Sampler (JAGS) packages rjags (103, 104) and runjags (105). We used three parallel chains of MCMC samplers, discarding the first 1,000 iterations as a burn-in and another 500 iterations to adapt before retaining the final 1,000 iterations to be analyzed for the posterior distribution. The model begins by using uninformative prior values (*SI Appendix*, Table S7), noting that the choice of prior does not affect the ultimate posterior distributions. We performed posterior predictive checks for the fit, mean, and SD to assess that the model choice and likelihood distribution are appropriate, finding that each fall within ±0.01 of 0.5 for Proxy$_{OH}$ (with ideal values falling as close as possible to 0.5; ref. 106). The MCMC chains for the Proxy$_{OH}$-[OH] slope and intercept parameters converge, as indicated by a Gelman–Rubin diagnostic between 1.000 and 1.005 for each spatial bin (a Gelman–Rubin diagnostic below 1.1 indicates convergence; ref. 107). We combine the posterior distributions across the three chains for 3,000 total values, per aircraft observation, to develop 95% credible intervals for the slope and intercept of the linear fit between the proxy and [OH].

Data, Materials, and Software Availability. Model simulations and analysis code have been deposited in Zenodo (https://zenodo.org/record/7512701) (108). All other study data are included in the article and/or supporting information.

Author affiliations: [a]Department of Earth and Environmental Sciences, Columbia University, New York, NY 10027; [b]Division of Ocean and Climate Physics, Lamont-Doherty Earth Observatory of Columbia University, Palisades, NY 10964; [c]Earth System Science Interdisciplinary Center, University of Maryland, College Park, MD 20740; [d]Atmospheric Chemistry and Dynamics Laboratory, National Aeronautics and Space Administration Goddard Space Flight Center, Greenbelt, MD 20771; [e]Department of Earth and Environmental Sciences, University of Rochester, Rochester, NY 14627; [f]Department of Earth System Science, University of California, Irvine, CA 92697; [g]Goddard Earth Sciences Technology and Research II, University of Maryland Baltimore County, Baltimore, MD 21250; [h]Goddard Earth Sciences Technology and Research II, Morgan State University, Baltimore, MD 21251; [i]National Aeronautics and Space Administration Goddard Institute for Space Studies, New York, NY 10025; [j]Cooperative Institute for Research in Environmental Sciences, University of Colorado Boulder, Boulder, CO 80309; [k]National Oceanic and Atmospheric Administration Chemical Sciences Laboratory, Boulder, CO 80305; [l]Department of Meteorology and Atmospheric Science, Pennsylvania State University, University Park, PA 16802; [m]Atmospheric Science Branch, National Aeronautics and Space Administration Ames Research Center, Moffett Field, CA 94035; [n]National Aeronautics and Space Administration Langley Research Center, Hampton, VA 23666; [o]Atmospheric Chemistry Observations & Modeling Laboratory, National Center for Atmospheric Research, Boulder, CO 80307; [p]National Oceanic and Atmospheric Administration Global Monitoring Laboratory, Boulder, CO 80305; and [q]Department of Earth and Planetary Sciences, Harvard University, Cambridge, MA 02138

Author contributions: C.B.B., A.M.F., S.M.L., J.M.N., G.M.W., L.T.M., R.C., M.J.P., D.C.A., B.N.D., and M.F.-C. designed research; C.B.B., S.M.L., J.M.N., G.M.W., G.C., M.F.-C., D.M.W., I.B., W.H.B., T.P.B., J.P.D., G.S.D., S.R.H., K.M., D.O.M., J.P., A.B.T., C.R.T., K.U., and S.C.W. performed research; C.B.B., A.M.F., S.M.L., J.M.N., G.M.W., R.C., M.J.P., D.C.A., B.N.D., and M.F.-C. analyzed data; A.M.F., S.M.L., J.M.N., G.M.W., L.T.M., R.C., M.J.P., D.C.A., and B.N.D. provided feedback; C.B.B., A.M.F., S.M.L., J.M.N., G.M.W., L.T.M., R.C., M.J.P., D.C.A., and B.N.D. edited manuscript drafts; G.C. provided technical support for the AM3 chemistry-climate model; I.B., W.H.B., T.P.B., J.P.D., G.S.D., S.R.H., K.M., D.O.M., J.P., A.B.T., C.R.T., K.U., and S.C.W. provided ATom instrument data; W.H.B., S.R.H., and K.M. provided feedback on manuscript drafts; and C.B.B., A.M.F., S.M.L., J.M.N., and M.J.P. wrote the paper.

The authors declare no competing interest.

This article is a PNAS Direct Submission. J.L. is a guest editor invited by the Editorial Board.

1. A. L. Rice et al., Atmospheric methane isotopic record favors fossil sources flat in 1980s and 1990s with recent increase. *Proc. Natl. Acad. Sci. U.S.A.* **113**, 10791–10796 (2016).
2. H. Schaefer et al., A 21st-century shift from fossil-fuel to biogenic methane emissions indicated by 13CH4. *Science* **352**, 80–84 (2016).
3. S. Schwietzke et al., Upward revision of global fossil methane emissions based on isotope database. *Nature* **538**, 88–91 (2016).
4. J. R. Worden et al., Reduced biomass burning emissions reconcile conflicting estimates of the post-2006 atmospheric methane budget. *Nat. Commun.* **8**, 2227 (2017).
5. R. L. Thompson et al., Variability in atmospheric methane from fossil fuel and microbial sources over the last three decades. *Geophys. Res. Lett.* **45**, 11499–11508 (2018).
6. M. Rigby et al., Role of atmospheric oxidation in recent methane growth. *Proc. Natl. Acad. Sci. U.S.A.* **114**, 5373–5377 (2017).
7. A. J. Turner, C. Frankenberg, P. O. Wennberg, D. J. Jacob, Ambiguity in the causes for decadal trends in atmospheric methane and hydroxyl. *Proc. Natl. Acad. Sci. U.S.A.* **114**, 5367–5372 (2017).
8. M. J. Prather, C. D. Holmes, Overexplaining or underexplaining methane's role in climate change. *Proc. Natl. Acad. Sci. U.S.A.* **114**, 5324–5326 (2017).
9. D. S. Stevenson, R. G. Derwent, O. Wild, W. J. Collins, COVID-19 lockdown emission reductions have the potential to explain over half of the coincident increase in global atmospheric methane. *Atmos. Chem. Phys.* **22**, 14243–14252 (2022).
10. Y. Zhao et al., Inter-model comparison of global hydroxyl radical (OH) distributions and their impact on atmospheric methane over the 2000–2016 period. *Atmos. Chem. Phys.* **19**, 13701–13723 (2019).
11. D. S. Stevenson et al., Trends in global tropospheric hydroxyl radical and methane lifetime since 1850 from AerChemMIP. *Atmos. Chem. Phys.* **20**, 12905–12920 (2020).
12. J. M. Nicely et al., A machine learning examination of hydroxyl radical differences among model simulations for CCMI-1. *Atmos. Chem. Phys.* **20**, 1341–1361 (2020).
13. L. T. Murray, A. M. Fiore, D. T. Shindell, V. Naik, L. W. Horowitz, Large uncertainties in global hydroxyl projections tied to fate of reactive nitrogen and carbon. *Proc. Natl. Acad. Sci. U.S.A.* **118**, e2115204118 (2021).
14. V. Naik et al., Impact of preindustrial to present-day changes in short-lived pollutant emissions on atmospheric composition and climate forcing. *J. Geophys. Res. Atmos.* **118**, 8086–8110 (2013).
15. O. Wild et al., Global sensitivity analysis of chemistry–climate model budgets of tropospheric ozone and OH: Exploring model diversity. *Atmos. Chem. Phys.* **20**, 4047–4058 (2020).
16. Q. Liang et al., Deriving global OH abundance and atmospheric lifetimes for long-lived gases: A Search for CH3CCl3 Alternatives. *J. Geophys. Res. Atmos.* **122**, 11914–11933 (2017).
17. S. A. Montzka et al., New observational constraints for atmospheric hydroxyl on global and hemispheric scales. *Science* **288**, 500–503 (2000).
18. S. A. Montzka et al., Small interannual variability of global atmospheric hydroxyl. *Science* **331**, 67–69 (2011).
19. P. K. Patra et al., Methyl chloroform continues to constrain the hydroxyl (OH) variability in the troposphere. *J. Geophys. Res. Atmos.* **126**, e2020JD033862 (2021).
20. P. K. Patra et al., Observational evidence for interhemispheric hydroxyl-radical parity. *Nature* **513**, 219–223 (2014).
21. M. Krol, P. J. van Leeuwen, J. Lelieveld, Global OH trend inferred from methylchloroform measurements. *J. Geophys. Res. Atmos.* **103**, 10697–10711 (1998).
22. R. Prinn et al., Atmospheric trends in methylchloroform and the global average for the hydroxyl radical. *Science* **238**, 945–950 (1987).
23. R. Prinn et al., Global average concentration and trend for hydroxyl radicals deduced from ALE/GAGE trichloroethane (methyl chloroform) data for 1978–1990. *J. Geophys. Res. Atmos.* **97**, 2445–2461 (1992).
24. G. M. Wolfe et al., Mapping hydroxyl variability throughout the global remote troposphere via synthesis of airborne and satellite formaldehyde observations. *Proc. Natl. Acad. Sci. U.S.A.* **116**, 11171–11180 (2019).
25. L. C. Valin, A. M. Fiore, K. Chance, G. González Abad, The role of OH production in interpreting the variability of CH2O columns in the southeast U.S. *J. Geophys. Res. Atmos.* **121**, 478–493 (2016).
26. S. C. Wofsy et al., ATom: Merged atmospheric chemistry, trace gases, and aerosols. (ORNL DAAC, Oak Ridge, Tennessee, USA, 2018). https://doi.org/10.3334/ORNLDAAC/1581 (Accessed 9 July 2021).
27. M. J. Prather et al., How well can global chemistry models calculate the reactivity of short-lived greenhouse gases in the remote troposphere, knowing the chemical composition. *Atmos. Meas. Tech.* **11**, 2653–2668 (2018).
28. C. R. Thompson et al., The NASA Atmospheric Tomography (ATom) Mission: Imaging the chemistry of the global atmosphere. *Bull. Am. Meteorol. Soc.* **103**, E761–E790 (2022).
29. G. M. Wolfe, M. R. Marvin, S. J. Roberts, K. R. Travis, J. Liao, The Framework for 0-D atmospheric modeling (F0AM) v3.1. *Geosci. Model Dev.* **9**, 3309–3319 (2016).
30. W. H. Brune et al., Exploring oxidation in the remote free troposphere: Insights from atmospheric tomography (ATom). *J. Geophys. Res. Atmos.* **125**, e2019JD031685 (2020).
31. W. H. Brune et al., Atmospheric oxidation in the presence of clouds during the Deep Convective Clouds and Chemistry (DC3) study. *Atmos. Chem. Phys.* **18**, 14493–14510 (2018).
32. X. Ren et al., HOx chemistry during INTEX-A 2004: Observation, model calculation, and comparison with previous studies. *J. Geophys. Res. Atmos.* **113**, D05310 (2008).
33. D. Davis et al., Marine latitude/altitude OH distributions: Comparison of Pacific Ocean observations with models. *J. Geophys. Res. Atmos.* **106**, 32691–32707 (2001).
34. D. O. Miller, W. H. Brune, Investigating the understanding of oxidation chemistry using 20 years of airborne OH and HO2 observations. *J. Geophys. Res. Atmos.* **127**, e2021JD035368 (2022).
35. J. B. Burkholder et al., Chemical Kinetics and Photochemical Data for Use in Atmospheric Studies. Evaluation No. 18 (2015).
36. H. Guo et al., Heterogeneity and chemical reactivity of the remote troposphere defined by aircraft measurements–Corrected. *Atmos. Chem. Phys.* **23**, 99–117 (2023).
37. J. Lelieveld, S. Gromov, A. Pozzer, D. Taraborrelli, Global tropospheric hydroxyl distribution, budget and reactivity. *Atmos. Chem. Phys.* **16**, 12477–12493 (2016).
38. C. M. Spivakovsky et al., Three-dimensional climatological distribution of tropospheric OH: Update and evaluation. *J. Geophys. Res. Atmos.* **105**, 8931–8980 (2000).
39. C. D. Holmes, M. J. Prather, O. A. Søvde, G. Myhre, Future methane, hydroxyl, and their uncertainties: Key climate and emission parameters for future predictions. *Atmos. Chem. Phys.* **13**, 285–302 (2013).
40. F. Rohrer, H. Berresheim, Strong correlation between levels of tropospheric hydroxyl radicals and solar ultraviolet radiation. *Nature* **442**, 184–187 (2006).
41. Y. Wang, D. J. Jacob, Anthropogenic forcing on tropospheric ozone and OH since preindustrial times. *J. Geophys. Res. Atmos.* **103**, 31123–31135 (1998).
42. L. T. Murray et al., Factors controlling variability in the oxidative capacity of the troposphere since the Last Glacial Maximum. *Atmos. Chem. Phys.* **14**, 3589–3622 (2014).
43. Q. Zhu, J. L. Laughner, R. C. Cohen, Combining machine learning and satellite observations to predict spatial and temporal variation of near surface OH in North American cities. *Environ. Sci. Technol.* **56**, 7362–7371 (2022).
44. M. A. Pimlott et al., Investigating the global OH radical distribution using steady-state approximations and satellite data. *Atmos. Chem. Phys.* **22**, 10467–10488 (2022).
45. H. M. Allen et al., H2O2 and CH3OOH (MHP) in the remote atmosphere: 2 physical and chemical controls. *J. Geophys. Res. Atmos.* **127**, e2021JD035702 (2022).
46. D. J. Cooper, Estimation of hydroxyl radical concentrations in the marine atmospheric boundary layer using a reactive atmospheric tracer. *J. Atmos. Chem.* **25**, 97–113 (1996).
47. A. S. Mahajan et al., Measurement and modelling of tropospheric reactive halogen species over the tropical Atlantic Ocean. *Atmos. Chem. Phys.* **10**, 4611–4624 (2010).
48. A. Badia et al., Importance of reactive halogens in the tropical marine atmosphere: A regional modelling study using WRF-Chem. *Atmos. Chem. Phys.* **19**, 3161–3189 (2019).
49. B. Tian et al., Evaluating CMIP5 models using AIRS tropospheric air temperature and specific humidity climatology. *J. Geophys. Res. Atmos.* **118**, 114–134 (2013).
50. J. H. Jiang et al., Evaluation of cloud and water vapor simulations in CMIP5 climate models using NASA "A-Train" satellite observations. *J. Geophys. Res. Atmos.* **117**, D14105 (2012).
51. IPCC, Climate Change 2013: The Physical Science Basis. Contribution of Working Group I to the Fifth Assessment Report of the Intergovernmental Panel on Climate Change, T. F. et al., Eds. (Cambridge University Press, Cambridge, United Kingdom and New York, NY, USA, 2013), pp. 1535.
52. V. O. John, B. J. Soden, Temperature and humidity biases in global climate models and their impact on climate feedbacks. *Geophys. Res. Lett.* **34**, L18704 (2007).
53. H. Su et al., Relationships of upper tropospheric water vapor, clouds and SST: MLS observations, ECMWF analyses and GCM simulations. *Geophys. Res. Lett.* **33**, L22802 (2006).

54. R. D. Cess *et al.*, Cloud feedback in atmospheric general circulation models: An update. *J. Geophys. Res. Atmos.* **101**, 12791–12794 (1996).

55. B. J. Soden, I. M. Held, An assessment of climate feedbacks in coupled ocean-atmosphere models. *J. Clim.* **19**, 3354–3360 (2006).

56. K. Riahi *et al.*, RCP 8.5–A scenario of comparatively high greenhouse gas emissions. *Clim. Change* **109**, 33–57 (2011).

57. S. Naus *et al.*, Constraints and biases in a tropospheric two-box model of OH. *Atmos. Chem. Phys.* **19**, 407–424 (2019).

58. R. R. Buchholz *et al.*, Links between carbon monoxide and climate indices for the southern hemisphere and tropical fire regions. *J. Geophys. Res. Atmos.* **123**, 9786–9800 (2018).

59. A. B. Thames *et al.*, Missing OH reactivity in the global marine boundary layer. *Atmos. Chem. Phys.* **20**, 4013–4029 (2020).

60. K. R. Travis *et al.*, Constraining remote oxidation capacity with ATom observations. *Atmos. Chem. Phys.* **20**, 7753–7781 (2020).

61. R. F. Silvern *et al.*, Observed NO/NO2 ratios in the upper troposphere imply errors in NO-NO2-O3 cycling kinetics or an unaccounted NOx reservoir. *Geophys. Res. Lett.* **45**, 4466–4474 (2018).

62. A. J. Turner, C. Frankenberg, E. A. Kort, Interpreting contemporary trends in atmospheric methane. *Proc. Natl. Acad. Sci. U.S.A.* **116**, 2805–2813 (2019).

63. C. L. Parkinson, Aqua: An Earth-Observing Satellite mission to examine water and other climate variables. *IEEE Trans. Geosci. Remote Sens.* **41**, 173–183 (2003).

64. L. N. Lamsal *et al.*, Indirect validation of tropospheric nitrogen dioxide retrieved from the OMI satellite instrument: Insight into the seasonal variation of nitrogen oxides at northern midlatitudes. *J. Geophys. Res. Atmos.* **115**, D05302 (2010).

65. B. N. Duncan *et al.*, A space-based, high-resolution view of notable changes in urban NOx pollution around the world (2005–2014). *J. Geophys. Res. Atmos.* **121**, 976–996 (2016).

66. A. Lorente *et al.*, Quantification of nitrogen oxides emissions from build-up of pollution over Paris with TROPOMI. *Sci. Rep.* **9**, 20033 (2019).

67. J. Ducker, C. D. Holmes, S. Kato, Using satellite-derived photolysis rates (SatJ) to evaluate constraints on atmospheric oxidants based on photolysis mechanisms in chemistry models. *Am. Geophys. Union Fall Meet. 2020 Abstr. A086-0011* (2020).

68. M. J. Prather, C. D. Holmes, J. Hsu, Reactive greenhouse gas scenarios: Systematic exploration of uncertainties and the role of atmospheric chemistry. *Geophys. Res. Lett.* **39**, L09803 (2012).

69. D. C. Anderson *et al.*, Spatial and temporal variability in the hydroxyl (OH) radical: Understanding the role of large-scale climate features and their influence on OH through its dynamical and photochemical drivers. *Atmos. Chem. Phys.* **21**, 6481–6508 (2021).

70. W. H. Brune *et al.*, Extreme oxidant amounts produced by lightning in storm clouds. *Science* **372**, 711–715 (2021).

71. J. Mao *et al.*, Global impact of lightning-produced oxidants. *Geophys. Res. Lett.* **48**, e2021GL095740 (2021).

72. W. H. Brune, D.O. Miller, A. B. Thames, *ATom: L2 Measurements from Airborne Tropospheric Hydrogen Oxides Sensor (ATHOS)* (ORNL DAAC, Oak Ridge, Tennessee, USA, 2019), https://doi.org/10.3334/ORNLDAAC/1709 (Accessed 9 July 2021).

73. I. C. Faloona *et al.*, A laser-induced fluorescence instrument for detecting tropospheric OH and HO2: Characteristics and calibration. *J. Atmos. Chem.* **47**, 139–167 (2004).

74. S. R. Hall, K. Ullmann, ATom: L2 Photolysis Frequencies from NCAR CCD Actinic Flux Spectroradiometers (CAFS) (ORNL DAAC, Oak Ridge, Tennessee, USA, 2019), https://doi.org/10.3334/ORNLDAAC/1714 (Accessed 9 July 2021).

75. R. E. Shetter, M. Müller, Photolysis frequency measurements using actinic flux spectroradiometry during the PEM-Tropics mission: Instrumentation description and some results. *J. Geophys. Res. Atmos.* **104**, 5647–5661 (1999).

76. T. B. Ryerson, C. R. Thompson, J. Peischl, I. Bourgeois, *ATom: L2 In Situ Measurements from NOAA Nitrogen Oxides and Ozone (NOyO3) Instrument* (ORNL DAAC, Oak Ridge, Tennessee, USA, 2019), https://doi.org/10.3334/ORNLDAAC/1734 (Accessed 9 July 2021).

77. I. Bourgeois *et al.*, Global-scale distribution of ozone in the remote troposphere from the ATom and HIPPO airborne field missions. *Atmos. Chem. Phys.* **20**, 10611–10635 (2020).

78. I. B. Pollack, B. M. Lerner, T. B. Ryerson, Evaluation of ultraviolet light-emitting diodes for detection of atmospheric NO2 by photolysis–Chemiluminescence. *J. Atmos. Chem.* **65**, 111–125 (2010).

79. T. B. Ryerson, E. J. Williams, F. C. Fehsenfeld, An efficient photolysis system for fast-response NO2 measurements. *J. Geophys. Res. Atmos.* **105**, 26447–26461 (2000).

80. G. S. Diskin, J. P. Digangi, ATom: L2 In Situ Atmospheric Water Vapor from the Diode Laser Hygrometer (DLH). (ORNL DAAC, Oak Ridge, Tennessee, USA, 2019), 10.3334/ORNLDAAC/1710.

81. G. S. Diskin, J. R. Podolske, G. W. Sachse, T. A. Slate, "Open-path airborne tunable diode laser hygrometer" in *Diode Lasers and Applications in Atmospheric Sensing* (International Society for Optics and Photonics, 2002), pp. 196–204.

82. R. Commane *et al.*, Atmospheric Tomography Mission (ATom) ATom: Measurements from the Quantum Cascade Laser System (QCLS) (ORNL DAAC, Oak Ridge, Tennessee, USA, 2020), https://doi.org/10.3334/ORNLDAAC/1747 (Accessed 9 July 2021).

83. R. Jimenez *et al.*, "Atmospheric trace gas measurements using a dual quantum-cascade laser mid-infrared absorption spectrometer" in *Novel In-Plane Semiconductor Lasers IV* (International Society for Optics and Photonics, 2005), pp. 318–331.

84. J. B. McManus *et al.*, A high precision pulsed quantum cascade laser spectrometer for measurements of stable isotopes of carbon dioxide. *J. Mod. Opt.* **52**, 2309–2321 (2005).

85. K. R. Chan, S. G. Scott, T. P. Bui, S. W. Bowen, J. Day, Temperature and horizontal wind measurements on the ER-2 aircraft during the 1987 Airborne Antarctic Ozone Experiment. *J. Geophys. Res. Atmos* **94**, 11573–11587 (1989).

86. S. E. Gaines, S. W. Bowen, R. S. Hipskind, T. P. Bui, K. R. Chan, Comparisons of the NASA ER-2 meteorological measurement system with radar tracking and radiosonde data. *J. Atmos. Ocean. Technol.* **9**, 210–225 (1992).

87. S. G. Scott, T. P. Bui, K. R. Chan, S. W. Bowen, The meteorological measurement system on the NASA ER-2 aircraft. *J. Atmos. Ocean. Technol.* **7**, 525–540 (1990).

88. S. C. Wofsy; ATom Science Team, *ATom: Aircraft Flight Track and Navigational Data* (ORNL DAAC, Oak Ridge, Tennessee, USA, 2018), https://doi.org/10.3334/ORNLDAAC/1613 (Accessed 9 July 2021).

89. M. E. Jenkin, J. C. Young, A. R. Rickard, The MCM v3.3.1 degradation scheme for isoprene. *Atmos. Chem. Phys.* **15**, 11433–11459 (2015).

90. J. M. Nicely *et al.*, An observationally constrained evaluation of the oxidative capacity in the tropical western Pacific troposphere. *J. Geophys. Res. Atmos.* **121**, 7461–7488 (2016).

91. E. Assaf *et al.*, The reaction between CH3O2 and OH radicals: Product yields and atmospheric implications. *Environ. Sci. Technol.* **51**, 2170–2177 (2017).

92. L. J. Donner *et al.*, The dynamical core, physical parameterizations, and basic simulation characteristics of the atmospheric component AM3 of the GFDL global coupled model CM3. *J. Clim.* **24**, 3484–3519 (2011).

93. J. Mao *et al.*, Sensitivity of tropospheric oxidants to biomass burning emissions: Implications for radiative forcing: Biomass burning on oxidants and forcing. *Geophys. Res. Lett.* **40**, 1241–1246 (2013).

94. C. B. Baublitz *et al.*, Sensitivity of tropospheric ozone over the Southeast USA to dry deposition. *Geophys. Res. Lett.* **47**, e2020GL087158 (2020).

95. D. M. Westervelt, A. M. Fiore, C. B. Baublitz, G. Correa, Impact of regional Northern Hemisphere mid-latitude anthropogenic sulfur dioxide emissions on local and remote tropospheric oxidants. *Atmos. Chem. Phys.* **21**, 6799–6810 (2021).

96. I. Bourgeois *et al.*, Large contribution of biomass burning emissions to ozone throughout the global remote troposphere. *Proc. Natl. Acad. Sci. U.S.A.* **118**, e2109628118 (2021).

97. M. Lin, Springtime high surface ozone events over the western United States: Quantifying the role of stratospheric intrusions: Stratospheric impacts on U.S. surface O₃. *J. Geophys. Res. Atmospheres* **117**, D00V22 (2012).

98. A. Guenther *et al.*, Estimates of global terrestrial isoprene emissions using MEGAN (Model of Emissions of Gases and Aerosols from Nature). *Atmos. Chem. Phys.* **6**, 3181–3210 (2006).

99. D. J. Rasmussen *et al.*, Surface ozone-temperature relationships in the eastern US: A monthly climatology for evaluating chemistry-climate models. *Atmos. Environ.* **47**, 142–153 (2012).

100. S. R. Hall *et al.*, Cloud impacts on photochemistry: Building a climatology of photolysis rates from the Atmospheric Tomography mission. *Atmos. Chem. Phys.* **18**, 16809–16828 (2018).

101. J. Kerckhoffs *et al.*, Mixed-effects modeling framework for Amsterdam and Copenhagen for outdoor NO₂ concentrations using measurements sampled with google street view cars. *Environ. Sci. Technol.* **56**, 7174–7184 (2022).

102. W. Sun *et al.*, Prediction of surface ozone episodes using clusters based generalized linear mixed effects models in Houston–Galveston–Brazoria area, Texas. *Atmos. Pollut. Res.* **6**, 245–253 (2015).

103. D. Lunn, D. Spiegelhalter, A. Thomas, N. Best, The BUGS project: Evolution, critique and future directions: The BUGS project. *Stat. Med.* **28**, 3049–3067 (2009).

104. M. Plummer, N. Best, K. Cowles, K. Vines, CODA: Convergence diagnosis and output analysis for MCMC. *R News* **6**, 7–11 (2006).

105. M. J. Denwood, runjags: An r package providing interface utilities, model templates, parallel computing methods and additional distributions for MCMC models in JAGS. *J. Stat. Softw.* **71**, 1–25 (2016).

106. M. Kéry, *Introduction to WinBUGS for Ecologists: A Bayesian Approach to Regression, ANOVA, Mixed Models, and Related Analyses* (Elsevier/Academic Press, ed. 1, 2010).

107. A. Gelman, D. B. Rubin, Inference from iterative simulation using multiple sequences. *Stat. Sci.* **7**, 457–472 (1992).

108. C. B. Baublitz, S. M. Ludwig, J. M. Nicely, G. M. Wolfe, Data, scripts and simulations for ProxyOH-[OH] analysis using ATom data and F0AM and AM3 simulations. Zenodo.org. https://zenodo.org/record/7512701. Deposited 1 August 2023.